JOURNAL OF AIRCRAFT
Vol. 40, No. 5, September–October 2003

Component-Based Empirical Model for High-Lift System Noise Prediction

Y. P. Guo* and K. J. Yamamoto†
The Boeing Company, Huntington Beach, California 92647
and
R. W. Stoker‡
The Boeing Company, Seattle, Washington 98124

This paper presents an empirical model for predicting noise from high lift systems, derived from a large database of airframe noise tests, involving various airplane models at various operating conditions. The model correlates noise not only to gross airplane parameters such as the dimensions of the high lift system and flight Mach number, but also to flow quantities that are physically responsible for the noise generation. Noise data used in the development of the model were acquired by using phased microphone arrays, which enables the decomposition of the total noise into components, relating the noise to the six individual components of the wing/high lift system. The methodology and results of this component-based model is presented, including source identification by source strength maps, component integration to derive far field spectra, validation/calibration of the integrated spectra by conventional free field microphone data, extrapolation of small-scale model test data to full-scale conditions with Reynolds number dependent scaling laws and the correlation between noise and flow quantities. Validations of the predictions with flight test data are also given to show the accuracy of the developed prediction tool.

Nomenclature

b	=	wing semispan
C_L	=	sectional lift coefficient
C_p	=	pressure coefficient
D	=	directivity factor
F	=	normalized spectrum
f	=	frequency
f_{full}	=	full-scale frequency
f_{small}	=	small-scale frequency
L	=	wing sectional lift
L_{full}	=	full-scale model dimension
L_{small}	=	small-scale model dimension
ℓ	=	length scale
M	=	freestream Mach number
p_s	=	surface pressure
p_0	=	mean pressure
R	=	radial distance
S	=	noise spectrum
Sr	=	Strouhal number
U	=	streamwise velocity
U_0	=	freestream velocity
V	=	spanwise velocity
α	=	wing angle of attack
Γ	=	vortex strength
γ	=	wing wake vorticity distribution
δ_F	=	flap deflection angle
δ_S	=	slat deflection angle
θ	=	directivity angle
ρ_0	=	mean density

Received 26 February 2003; revision received 10 June 2003; accepted for publication 17 June 2003.

*Engineer, Boeing Phantom Works. Member AIAA.
†Engineer, Boeing Phantom Works. Member AIAA.
‡Engineer, Boeing Commercial Airplane Company. Member AIAA.

I. Introduction

EMPIRICAL models have long been used for airframe noise prediction.[1–5] These models usually rely on the test data available and the understanding of the source mechanisms. In recent years, there has been much research on airframe noise with significant progress in many aspects, including the understanding of physical sources[6–14] and the use of advanced measurement techniques such as phased microphone array.[15–17] This has led to the development of improved prediction tools that are more physics based. In this paper, we present such a development. In comparison with previous empirical models for high-lift system noise prediction, the present model differs in two main aspects: It is component based, and the noise from the components is related to flow quantities as well as gross geometry parameters. The former is made feasible by the development of the phased microphone array for airframe noise measurements and the latter results from our improved understanding of the source mechanisms of aircraft high-lift systems.

Our empirical model is developed from a large acoustic database consisting of elliptic mirror data for the Boeing 737, 757, and 777 airplanes and phased microphone array data for the Boeing 767, DC-10, and MD-11 airplanes. The elliptical mirror data are the database used by The Boeing Company to develop an early version of component-based prediction models,[5] whereas the phased array data have been made available only recently. The data are acquired in a series of tests in the Boeing Low Speed Aeroacoustic Facility (LSAF), the NASA Ames Research Center 40 × 80 ft wind tunnel, and the NASA Ames Research Center 12-ft pressure wind tunnel. For all of the models, the test conditions involve variations in wind-tunnel flow Mach number, model angle of attack, flap angle, slat angle, and landing gear on and off. The details of the tests, including test setup, test matrix, model geometry, and data acquisition and reduction, have been previously reported[5–7,15,18–20] so that will not be repeated here. In all of the tests, the measurements were done at locations corresponding to the overhead direction in aircraft flight test, which is the direction with the most significant airframe noise contribution.

One of the main advantages of using phased array measurements and elliptical mirror data, instead of the traditional free-field microphone data, is that the total noise can be decomposed into subcomponents. This is feasible because the beam-forming technique used in the array data processing leads to source distributions on the aircraft high-lift system. When the aircraft surface is divided

into subregions according to the source distribution and the sources are integrated over these subregions, noise components from different subregions can be derived. This component-based approach is not feasible with only free-field microphone data because the measurements from those microphones contain contributions from all sources, and these sources are aerodynamically interrelated to each other, making it very difficult to separate one from the other. The integration of phased microphone array data to derive far-field spectra is, however, by no means a mature, standard procedure. It still involves many unresolved issues.[15–17] For example, it is known that phased array measurements do not give absolute source levels and that the integration is sensitively subject to side-lobe contamination, especially in cases of multiple sources of comparable amplitudes. These are issues still under research. It is then important in developing empirical models from phased array data to calibrate phased array measurements with other conventional measurement techniques such as free-field microphone. For this purpose, some of the tests in our database were done with both phased microphone array measurements and conventional microphone measurements, and it will be shown that the methodology used in integrating the phased array data gives results that are consistent with single-microphone data.

It is also important to calibrate small-scale model test data with full-scale test data to ensure the noise sources are scalable. This is especially important for small models less than about 10% of the full-scale model, in which case, possible Reynolds number effects may alter the flow features between the two model scales, rendering different source mechanisms for the model scale compared to the full scale.[6,18] Because of this, the noise data from small-scale model tests may not be scaled to full-scale conditions by the conventional extrapolation methodology that basically involves scaling down the frequency and scaling up the amplitude according to the model size ratio. In this case, a Reynolds number-dependent scaling should be applied. As is well known, the dependence of the sound-generating flow features on the Reynolds number is very complex and not well understood. There is very little theoretical work on this topic. In this paper, we use an empirical correction[6] and will show that it reconciles small-scale data with full-scale measurements very satisfactorily. Note that the difference between small-scale and full-scale model test data and the need for corrections in addition to the conventional geometry-based extrapolation by themselves do not conclusively demonstrate the Reynolds number effects. The discrepancy in the scaling may also be due to other causes. We call these Reynolds number effects only as a hypothesis and regard it as a possible explanation for the discrepancy shown by the data. For the development of empirical tools, however, the corrections seems to work fine, although further research is apparently needed to further our understanding of the Reynolds number effects on airframe noise sources.

Features in the flow around the aircraft generate airframe noise. It is then intuitively desirable to establish the cause-and-effect relation between the noise and the quantities that control the noise generating flow features. This is an important aspect of the noise prediction model presented in this paper, where each noise component in the high-lift system is correlated to aerodynamic quantities that describe the flow for each component, in addition to the overall geometry and flow parameters. This renders the approach more physics based, and we think that this is an important step forward from existing empirical models for airframe noise prediction, which almost exclusively use the overall geometry and flow parameters only in the prediction. The noise–flow correlation is helped by recent progress in understanding airframe component noise sources, which guide the selection of aerodynamic quantities for the correlation analysis. A good example is the flap side-edge noise component. Whereas some existing airframe noise models assume that the dominant noise comes from the wing trailing edge,[1,2,10] recent research has shown that this may not be the case. Instead, flap side-edge flow may be a significant airframe noise source, and the source mechanism is strongly related to the side-edge vortex,[6,7,9,11–14] which is a result of the crossflow separation at the side edge due to the large aerodynamic loading on the flap. The phased array data show that this is indeed a significant noise component and that it is correlated to parameters such as the strength of the side-edge vortex and the crossflow velocity. These quantities are readily derived from panel method calculations [or can be found by any other aerocalculations such as computational fluid dynamics (CFD)].

In the following sections, the process of the data analysis, the identification of component sources, the derivation of the far-field component noises and their correlation with flow parameters are described in detail. The validation of the derived noise prediction tools is also discussed and comparisons are made with free-field measurements from both small-scale and full-scale tests.

II. Component Sources

The source maps from the phased microphone array and the elliptic mirror can be used to identify major sources and, hence, to define subregions for the source integration. Source maps are the results of the beam-forming data processing. All our tests are done in wind tunnels and there is no relative motion between the aircraft model and the microphones. In this case, it is conventional to use frequency-domain beam forming, which is a standard and very straightforward procedure.[15–17] The results of the data processing give the relative source strengths on the beam-forming grids, which are chosen to be the wing surface.

To illustrate the beam forming results, Fig. 1 shows the source distribution for a 4.7% MD-11 semispan model at 10 kHz. The test was done at NASA Ames Research Center in the 12-ft pressure wind tunnel, where the phased microphone array was mounted on the wind-tunnel wall, looking at the underside of the wing.[18,19] The test conditions shown in Fig. 1 are the flow Mach number $M = 0.207$ and the flaps and slats deployed at 35 and 20 deg, respectively. For this example, the source map shows dominant sources at the two flap side edges. Other sources with relatively smaller amplitudes are also seen at the leading-edge slat locations and the trailing-edge locations of the wing/flap system away from the flap side edges.

To quantify the relative importance of the sources at different locations further, we choose a few cuts on the source map and plot the source strengths along these cuts. The cut locations are shown in Fig. 1, and the source strengths along these cuts are given in Fig. 2. Cut 1 goes through the dominant source at the inboard edge of the flap. The source strength plot (Fig. 2c) clearly shows the dominance of this source. Along this cut, the flap side-edge source is at least 10 dB stronger than the background. The slat noise source is also clearly seen in Fig. 2c, which is about 6 dB lower than the flap-edge source, but is still well above the background. When the cuts are taken at other locations, other sources are revealed very clearly. Cut 2 (Fig. 2b) is at the middle span location and shows both the slat source and the trailing-edge source. At this location, the amplitudes of these two sources are quite comparable. Fig. 2a is the cut at the outboard flap side edge. Similarly to the inboard flap edge, the noise

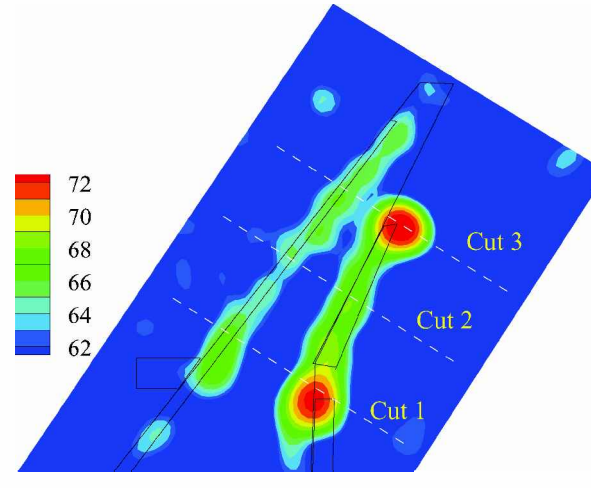

Fig. 1 Airframe noise source distribution example derived from phased microphone array measurements: 4.7% MD-11, M = 0.207, δ_F = 35 deg, δ_S = 20 deg, and f = 10,000 Hz.

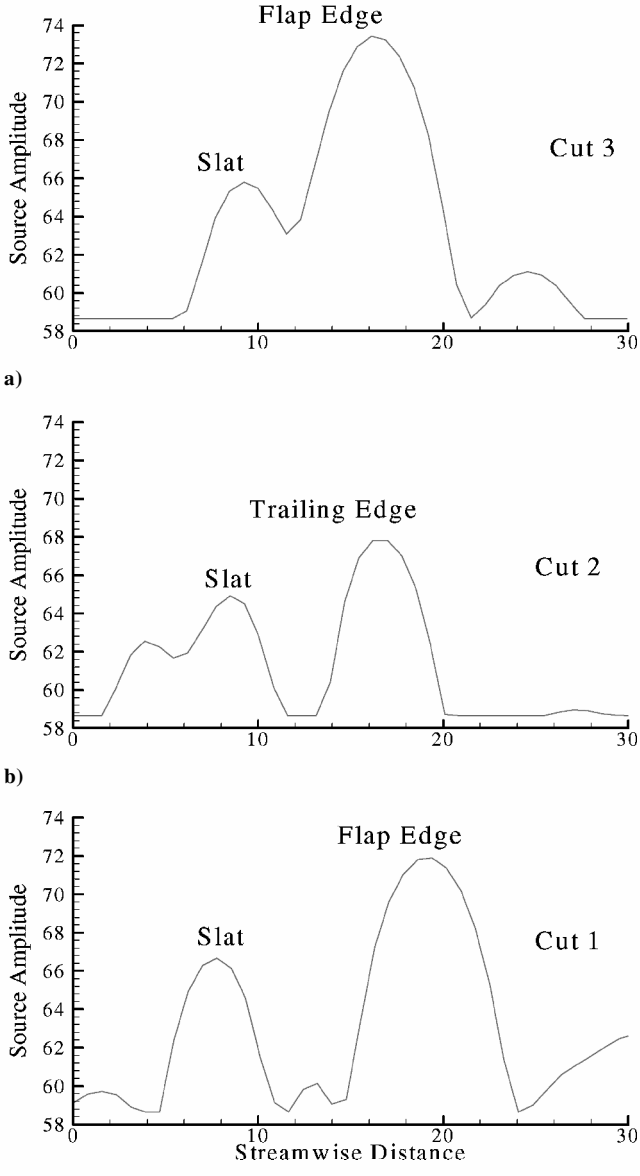

Fig. 2 Source strengths at three locations along the wing span: dominant sources at the flap edges, the slats, and the trailing edges for locations shown in Fig. 1.

source along this cut is dominated by the flap side edge, though the slat source is also seen here.

From the source strength plots in Fig. 2, it is clear that the sources at the flap side edges have much higher amplitudes than those at other locations, such as the slat and the trailing edge. This, however, does not necessarily mean that the other sources are less important. This is because, although the other sources may have weaker strengths, they may have a much larger source area than the flap side-edge sources, which are usually very concentrated. The far-field noise is determined by the integration of the source strength over the source area. Thus, a weaker source distribution with a larger source area may lead to more noise in the far field. The source strengths are also frequency dependent; the dominant sources at one frequency may become less important at other frequencies.

Based on the analysis of the source maps and the source strengths at different locations, we divide the wing area into subregions for the component analysis. The subregions are used for source integration to derive far-field spectra. They also correspond to subcomponents of the wing/high-lift system, each of which may have different noise-generation mechanisms. There are altogether six components, namely, the leading-edge slat, the outboard flap edge, the inboard flap edge, the trailing edge, the high-speed aileron, and a residue

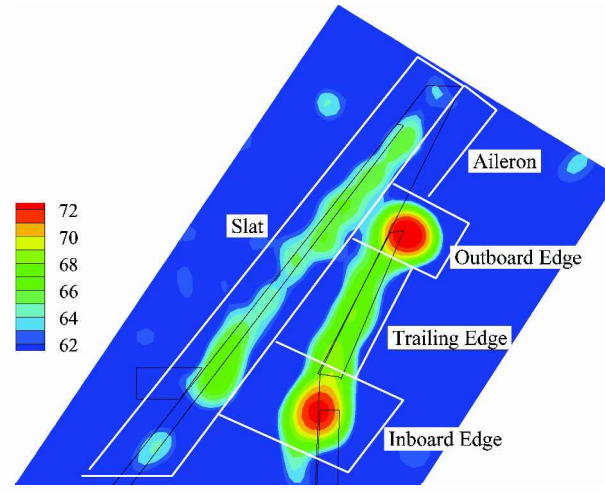

Fig. 3 Subregion definitions example for source strength integration to derive the noise spectra: 4.7% MD-11, M = 0.207, δ_F =35 deg, δ_S = 20 deg, and f = 10,000 Hz.

noise floor. An example of the definitions for the subregions is given in Fig. 3 for the MD-11 data shown in Figs. 1 and 2. For other models, the subregions are similarly defined. It is appropriate to point out that this definition of subregions does involve a certain degree of arbitrariness, especially in the shapes and sizes of the subregions. For example, the high-speed aileron component is defined as a rectangular region close to the wing tip. This region actually contains some trailing-edge sources. It is not further divided for the sake of simplifying the computations. The arbitrariness in the definition of the subregions, however, does not pose a severe limitation on the analysis for two reasons. The first is that the subregions are always required to cover the entire wing area so that the sum of the noise components is always equal to the total noise of the wing, though the noise components themselves may vary with different definitions of the subregions. The second reason is that the subregions are required to contain the respective dominant sources in the regions. Because the dominant sources are much stronger than other sources within each subregion, the variations in shape and size of the subregion definition is not very critical in the source strength integration. The integration is dominated by the major sources. Note also that the locations and the sizes of the subregions are frequency dependent. As frequency varies, the source characteristics also change. Thus, the decomposition of the sources should also change with frequency.

III. Integrated Spectra

As discussed in the Introduction, there is no unique and reliable way of deriving the far-field noise spectra from the phased array beam-forming results. The procedure is, thus, highly empirical and requires calibration with results from free-field microphones. From the theory of beam-forming data processing, the source maps only give relative strengths of the sources at the grid points. The result for a beam-forming grid is the coherent addition of the noise levels from the source at that grid point, seen by the microphones in the array. Thus, it is intuitive to postulate that the noise level for a single microphone can be simply approximated by the beam-forming result divided by the number of microphones in the array. The noise level for a single microphone due to sources in a region can then be found simply by integrating the results over the region.

This would work well for very concentrated sources with arrays of high resolution so that the integration does not pick up side-lobe contributions. For most practical applications, however, the sources are very likely to be distributed, such as the slat sources, and the array resolution is always limited and frequency dependent. In this case, the side lobes of the beam-forming results can contaminate the integration. To overcome this difficulty, we divide the integrated results by a calibration integral, which is basically the response of the array to an ideal, concentrated point source of unit strength. Because the ideal source and the real sources are likely to generate

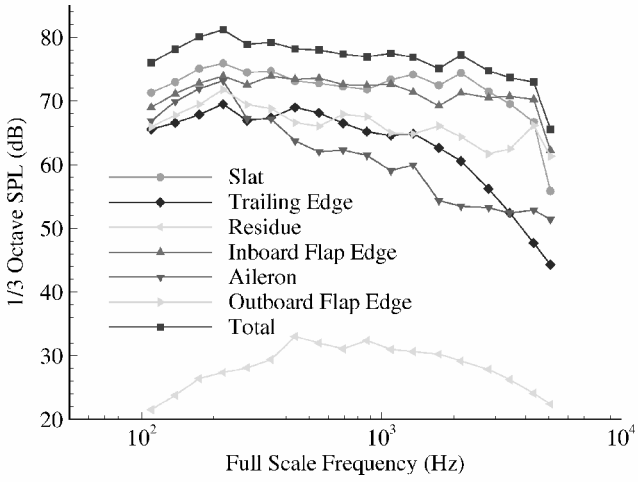

Fig. 4 MD 11 airframe noise spectra example for different components, integrated from phased array measurements.

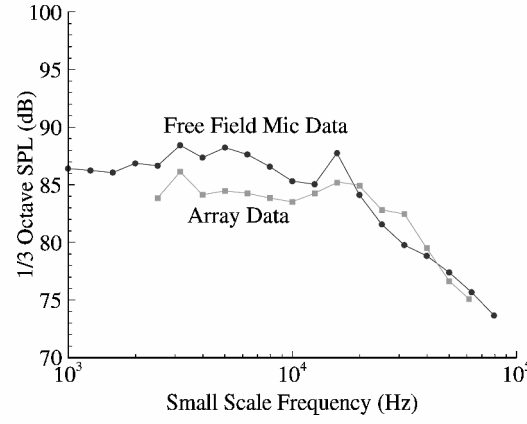

Fig. 5 Comparison between free-field microphone data and array integrated spectra for 4.7% MD-11 aircraft model.

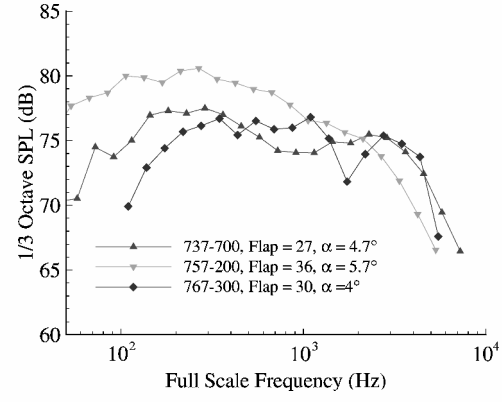

Fig. 6 Comparison of the integrated spectra of inboard flap side-edge sources for different airplane models.

comparable side lobes when viewed by the same array, the use of the calibration integral eliminates, or at least reduces, the contributions in the integrated spectra due to the side lobes. To further reduce the side-lobe contamination in the integration, a local maximum is identified within each subregion at each frequency so that contributions more than 6 dB below the local maximum are ignored in the integration. This works well for subregions that contain dominant sources with well-defined local maximum, such as the flap side edges and the slat region. For subregions with no apparent dominant source, such as the residue component and the high-speed aileron component at some frequencies, the 6-dB cutoff may include some side-lobe contributions in the integration, which causes spectral buildup in the far-field spectra, especially at high frequencies. This in turn may affect the total noise when the components are added. When this happens, the spectral buildup must be corrected by imposing a falloff with frequency. The precise form of the falloff is not critical because the components that need correction are usually not the dominant components; their contributions to the total noise are usually not significant. Clearly, this is an empirical approach to establish the relation between the source integration and the far-field spectra, and it is important to validate the integrated results with data from other conventional measurement techniques, such as free-field microphones.

With this procedure, the far-field noise spectra for each of the six subcomponents defined in the preceding section can be derived. Some examples of the integrated component spectra are shown in Fig. 4, for the same MD-11 model and flow conditions as those for Fig. 1. In Fig. 4, the noise spectra for all six components, plus the total, are plotted in full-scale frequencies. The procedure for extrapolating the small-scale data to full scale will be discussed in the next section. For the examples shown in Fig. 4, the most dominant sources are the slat and the inboard flap side edge (circles and the triangles). The two have very comparable amplitudes in the midfrequency domain from about 200 to 2000 Hz, which is an important frequency domain for aircraft noise certification. Below this frequency domain, the slat is 1–2 dB noisier than the inboard flap side edge, and at high frequencies, the slat generates less noise. Following these two most dominant sources is the outboard flap side edge and the trailing-edge component, which are comparable in amplitude for frequencies up to about 1000 Hz. Above that, the trailing-edge noise falls off very rapidly. Figure 4 also shows that the high-speed ailerons do not generate much noise, and the residue noise is tens of decibels below the others, meaning that the five high-lift system component subregions essentially capture all of the noise.

Note that some of the seemingly weak sources shown in Fig. 1 integrate to very significant noise spectra. The component with highest amplitude in Fig. 4 is the slat noise, which is weak in Fig. 1 compared with the flap side-edge sources. This is because the spectra are the integrated results. Although the slat sources have smaller amplitudes than the flap sources, they are more widely distributed. The former basically occupies the entire slat region, whereas the latter is highly concentrated in the flap side-edge region. The same happens to the trailing-edge noise. From Fig. 1, it can be seen that trailing-edge noise amplitude is much lower than that of the outboard flap side edge, but when integrated, the two become comparable for frequencies below about 1000 Hz.

Note that the ordering of the relative importance of the component noise sources shown in Fig. 4 is by no means universal. It depends on the flow conditions and the high-lift configurations. The MD-11 aircraft is known to have heavily loaded flaps so that, when the flaps are deployed at maximum angle, which is 50 deg, flap noise will become the dominant component and overwhelm others.[7,18–20] This is not the case for the results in Fig. 4 because the flaps in this case are at 30 deg, while the slats are fully deployed, which lowers the flap noise and makes the slats the most significant noise component. In general, the relatively old aircraft types, such as the MD-11 and the Boeing 757, which usually have heavy flap loading, generate more flap noise. The newer types, such as the Boeing 777, which has more advanced flap design, generate more slat noise.

As discussed in the Introduction, calibration is a crucial step in developing empirical tools from phased array data. This is to ensure that the spectra integrated from phased array beam-forming data indeed represent the far-field noise. The calibration can be done with free-field microphone measurements, one example of which is presented in Fig. 5 for a 4.7% MD-11 model, for which free-field microphone data are available, obtained from an earlier test in the NASA Ames Research Center 40 by 80 ft wind tunnel.[7,20] The comparisons are satisfactory for both the spectral shapes and the absolute amplitudes. Comparisons are also made for other models in our database, and similar accuracy is seen in those comparisons. Another kind of calibration can be done by comparing results for different models, as shown as an example in Fig. 6 for the Boeing

737, 757, and 767. Figure 6 shows the inboard flap edge source. The data for the first two models (the Boeing 737 and 757) are from the elliptic mirror measurements, whereas those for the Boeing 767 model are from the integrated phased microphone array. Evidently, both the spectral shapes and the absolute levels of the spectra show quite reasonable comparison, validating the method for deriving the spectra from beam-forming source maps.

IV. Extrapolation to Full Scale

According to conventional procedures,[5,20,21] the critical parameter in extrapolating small-scale model test data to full scale is the ratio of the model dimension to that of the full-scale aircraft. This ratio is important because both frequencies and amplitudes are scaled by it. The extrapolation procedure is quite straightforward and has been previously described. Thus, it will be described here only very briefly. The process basically involves first extrapolating the measured wind-tunnel data from the microphone locations to unit distance from the assumed source location. This essentially scales out the effects of spherical spreading, as well as atmospheric absorption under the test day conditions. The second step is then to scale the results at unit distance from the source from small scale to full scale, which involves scaling the frequencies down and amplitudes up, both by the model dimension ratio. The scaled data are then extrapolated to the far field, typically the certification distance of 394 ft away from the aircraft center. By doing so, the losses due to spherical spreading and atmospheric absorption at standard acoustic day conditions are taken into account.

Following this procedure, the small-scale data can be extrapolated to full scale at certification conditions. The extrapolated results, however, do not agree well with full-scale measurements, for example, the MD-11 model shown in Fig. 7. The comparison between the extrapolated results and the flight data is between the triangles and the squares. The comparisons in Fig 7 are reasonably good for frequencies below about 500 Hz, but show significant discrepancies for higher frequencies. The extrapolated data significantly underestimate the fly-over data in the middle- and high-frequency regions by as much as 10 dB, which is unacceptable. From the acoustic data alone, we cannot conclusively understand the reasons for these large discrepancies. One hypothesis is that the small scale of the model aircraft may cause quite different flow behavior from that of the full-scale aircraft, as is commonly described as Reynolds number effects.[6,18] Because of the extremely complex relation between the Reynolds number and the sound generating features of the flow, much research is clearly needed to gain a better understanding of this issue. However, it is clear from Fig. 7 that corrections are needed to rectify these effects when using the small-scale data, no matter what the cause of these effects is.

An attempt to derive a correction for the Reynolds number effects has been made recently.[6] In this case, we argue that the dominant length scale in the flow should be dependent on the Reynolds number, instead of the physical dimension of the model aircraft. There are many cases in which the flow is governed by a length scale dependent on the flow conditions, turbulent boundary-layer flow being a typical example where the thickness of the boundary layer is determined by the local Reynolds number (see Ref. 22). If this idea holds for the flow surrounding the high-lift system of the aircraft, it implies that the procedure for the extrapolation from small to full scale should be modified. In particular, the length-scale extrapolation should depend on the flow conditions, as well as the physical dimensions of the models. One consequence of this is a quite different frequency scaling law from that in the conventional approach described earlier in this section.

This scaling law can be derived by equating the Strouhal number in the small-scale model experiments to that in the full-scale test, with the Strouhal number in both cases being based on a length scale that is flow dependent, such as the momentum thickness of the turbulent boundary layer. These flow-dependent length scales can be approximated from the first principles of boundary flows,[6] and the frequency extrapolation law can be found as

$$f_{\text{full}}/f_{\text{small}} = (L_{\text{small}}/L_{\text{full}})^{2-\gamma} \tag{1}$$

where the subscripts full and small indicate quantities in full-scale and small-scale tests, respectively, and L is the physical dimension of the model. The value of γ ranges from 1.1 to 1.2, depending on flow conditions. The upper bound $\gamma = 1.2$ corresponds to the case of a fully developed turbulent boundary layer.

This shows that the frequencies of full-scale tests and small-scale model experiments are related by the physical scale factor of the models to a power that is less than one, in contrast to the commonly used linear dependence and is independent of the Reynolds number. The Reynolds number related frequency scaling (1) is especially important when very small models are used to simulate full-scale models. In our MD-11 small-scale model tests, for example, the scale factor of the physical models is 0.047, which, according to the result (1), gives a frequency-scaling factor of 0.0866 if γ is taken to be 1.2. This is almost twice the physical scale factor of 0.047 and can quite significantly affect the spectra when small-scale model test data are extrapolated to full-scale conditions. To demonstrate this point, Fig. 8 shows the full-to-small scale frequency ratio as a function of the physical dimension ratio, both for the conventional scaling and the Reynolds number dependent scaling (1). It is clear from Fig. 8 that the differences between the two can be quite significant for small-model tests. For practical applications, Fig. 8 indicates that for models larger than about 10% of the full-scale aircraft, the conventional frequency scaling may be sufficient, but for models less than about 10% of the full-scale geometry, frequencies have to be scaled according to the Reynolds number dependent scaling.

Reynolds number effects can also affect the amplitude scaling, for which there is little research and information available. To proceed with our empirical tool development, we rely on an empirical

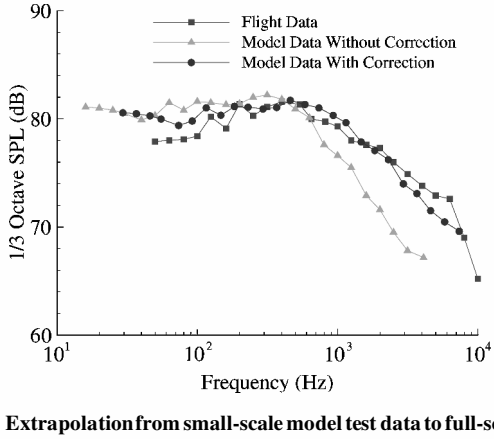

Fig. 7 Extrapolation from small-scale model test data to full-scale configurations for 4.7% MD-11 aircraft model, showing the importance of Reynolds number dependent corrections.

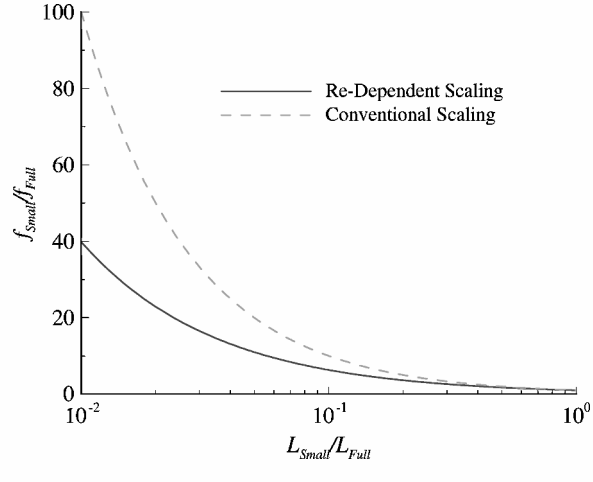

Fig. 8 Reynolds number dependent frequency scaling, compared with conventional scaling.

correction derived from tests in pressurized wind tunnels.[18,19] With the corrections, the comparison between the extrapolated data and flight data can be greatly improved. This is also demonstrated in Fig. 7 by the circles. Clearly, the comparison between small-scale data and full-scale data becomes much more satisfactory when the Reynolds number corrections are applied. Although the frequency scaling (1) does have sound physical reasoning and the corrected comparison in Fig. 7 shows good agreement with full-scale flight data, we emphasize again that the Reynolds number effects are a hypothesis that needs further validation and confirmation. In any event, it can be regarded as an empirical correction, which serves the purpose of this paper, namely, to develop empirical tools for airframe noise prediction.

V. Aerodynamic Parameters for Correlation Analysis

In the preceding sections, we discussed some issues related to the data reduction, ranging from subregion integration to derive the far-field noise spectra from the phased array data to the extrapolation from small-scale model data to full scale. Once the procedures are established for the data reduction, a database of noise spectra is developed for each of the six components of the high-lift system. The database consists of a total of 233 noise data sets, including many airplane models with variations in both configurations and flow conditions. Table 1 summarizes the database. For most phased array measurements, the array is located in the overhead location (90 deg). In addition to phased array and elliptical mirror data, we also have free-field microphone data and flight data, which are used for calibration and validation.

With the noise spectra derived for the components, the next step is to correlate them to the controlling geometric, operational, and aerodynamic quantities. Geometric parameters include the dimensions of the components, such as the chord length, the span, and the thickness. Operational parameters are those such as the angle of attack and the angle of deployment. There are common flow quantities for all of the components, such as the freestream flow Mach number. Each component also has unique flow quantities, which are identified by analyzing each noise source separately. For flap side-edge sources, for example, the side-edge vortex strength and the crossflow velocity are two quantities that are unique to these sources.

The correlation analysis is to derive relations between the far-field noise spectra and the flow and geometry parameters. To this end, we assume a functional dependence, for each component, between the noise spectrum and the geometric, operational, and aerodynamic parameters of the form

$$S = S_0 F(Sr) D(\theta) M^{b_1} C_L^{b_2} (\ell/r)^{b_3} (\sin\alpha)^{b_4} (\sin\delta)^{b_5} \tag{2}$$

Here S is the noise spectrum for a particular component, and S_0 is a constant. The frequency dependency of the noise is given by the normalized spectrum $F(Sr)$ in terms of the Strouhal number,

$$Sr = f\ell/U_0 \tag{3}$$

with ℓ a length of the component, its thickness, for example. The directivity of the noise is given by the directivity factor $D(\theta)$, where θ is the directivity angle in the flyover plane, and the spectrum is assumed to be proportional to some powers of all of the other parameters, which include the flow Mach number $M = U_0/c$, with c the constant sound speed, the angle of attack α, the sectional lift coefficient of the component C_L, the deflection angle of the component δ, and the length of the component normalized by the far-field microphone distance r. These are the parameters common to all of the components. For each particular component, parameters unique to that component are to be added to the general expression (2). For example, the strengths of the side-edge vortex and the velocity of the span-wise crossflow are added for the flap side-edge noise sources. Similarly for the slat noise sources, the vortex strengths in the cove region, the velocity of the flow in the gap between the slat trailing edge and the main wing and the width of the gap are added. As indicated in the general expression (2), the dependencies of the noise spectra on these parameters are assumed to be of the simple form of a power law. The indices of the power laws ($b_1, b_2, b_3, \ldots$) are to be determined by the regression analysis of the database.

Table 1 Model configurations and flow conditions in the acoustic database

Airplane model	Mach number	Angle of attack	Flap angle
737-300	0.18, 0.2, 0.22, 0.24	0, 4.7, 6.7, 8.7	25, 27, 30
737-700	0.2, 0.24	0, 4, 6, 8	25, 30, 40
757	0.18, 0.2, 0.22, 0.24	0, 5.7, 7.7, 9.7	20, 25, 36
767	0.2, 024	0, 2, 4, 6, 8, 10, 12, 14	30
777	0.2, 0.24	0, 7.34, 9.34	30
DC-10	0.21, 0.26, 0.28	4.7	25, 35, 50
MD-11	0.26, 0.28	4.7	35, 50

The regression analysis is basically to correlate the acoustic data to the geometrical, operational, and aerodynamic quantities. The aerodynamic quantities include the static loading on the high-lift system components (slats, flaps, and ailerons). To find this, potential flow panel methods are used for all of the models, which are known to give reasonably accurate loading calculations and are the methods routinely used in aircraft design. In applying the results developed here, other aerocalculation methods such as CFD can also be used to derive the flow parameters. The potential flow panel method is chosen here because of its computational efficiency. Needless to say, it would be very costly to do CFD calculations for all of the airplanes and for all of the configurations in our database.

The drawback of using the potential flow methods for the aerodynamic calculations is that there are quantities that are needed for the regression analysis but are not directly given by the panel code calculations. For these parameters, simple derivations are done to compute their values. One such parameter is the side-edge vortex strength at flap side edges. From the definition of the side-edge vortex, it is given by the jump in the wake vorticity distribution across the side-edge location, namely,

$$\Gamma = \gamma_2 - \gamma_1 = \Delta\gamma(\eta) \tag{4}$$

where Γ is the strength of the side-edge vortex, $\gamma(\eta)$ is the wake vorticity distribution along the nondimensional spanwise coordinate η (physical distance divided by the semispan), and the subscripts 1 and 2 denote the two locations on the left and right sides of the side edge, respectively (Fig. 9). From aerodynamics, it is known that the wake vorticity is related to the wing lift by

$$L(\eta) = \rho_0 U_0 \gamma(\eta) \tag{5}$$

where L is the sectional lift (lift per unit span) and ρ_0 is the constant mean density. From this, the side-edge vortex strength (4) can be related to the lift by

$$\Gamma = \Delta L(\eta)/\rho_0 U_0 \tag{6}$$

When the definition of the sectional lift coefficient is used further, this can be rewritten as

$$\Gamma = 2bU_0 \Delta C_L \tag{7}$$

which relates the side-edge vortex strength to the semispan b of the flap, the freestream velocity U_0, and the jump in the sectional

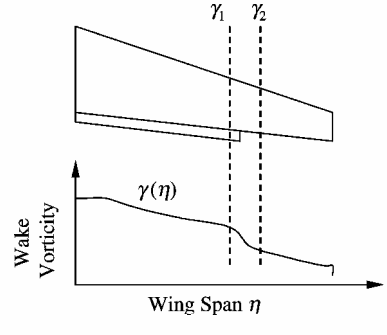

Fig. 9 Definition of flap side-edge vortex.

lift coefficient across the flap side edge. The last quantity can be derived directly from the panel code calculation or any other CFD calculations.

Another flow parameter that is correlated to the noise for the flap side-edge component is the velocity of the spanwise crossflow, which needs to be estimated from the results of aerocalculations. This velocity can be related to the velocity of the steady potential mean flow on the flap surface away from the side edge. From the theory of potential flows, it is known that the velocity near the flap side edge decreases away from the edge. We argue that this potential flow behavior only occurs in the immediate vicinity of the side edge, probably on the order of the local flap thickness, where the static loading difference between the upper and the lower surface is not significant. Away from the side-edge region, the crossflow is driven by the loading on the flap. Thus, we assume that the crossflow velocity is maintained at V by the loading difference on the flap. In this region, the total velocity is the sum of the crossflow and the chordwise mean flow originating from upstream. The application of the Bernoulli equation then leads to

$$p_s + (\rho_0/2)(U^2 + V^2) = p_0 + (\rho_0/2)U_0^2 \tag{8}$$

where U and V are the velocity on the flap surface in the chordwise and the spanwise direction, respectively, p_s and p_0 are the pressure on the flap surface and at infinity, respectively, and U_0 is the constant freestream velocity at infinity. When the definition for the pressure coefficient

$$C_p = (p_s - p_0)\Big/\left(0.5\rho_0 U_0^2\right) \tag{9}$$

is used, Eq. (8) can be rewritten as

$$V^2\Big/U_0^2 = 1 - C_p - U^2\Big/U_0^2 \tag{10}$$

where C_p is a function of the chordwise coordinate. When the flap is deployed, the streamwise flow is bent to follow the flap. Thus, we write

$$U = U_0 \cos(\alpha + \delta_F)(1 - C_p) \tag{11}$$

where α is the angle of attack of the main wing. With this substituted into Eq. (10), we find that

$$V = \left\{ \sin^2(\alpha + \delta_F) + C_p \cos^2(\alpha + \delta_F) \right\}^{\frac{1}{2}} (1 - C_p)^{\frac{1}{2}} U_0 \tag{12}$$

Through this, the crossflow velocity V is related to the aerodynamic properties of the flap, as well as the geometry parameters. Note that, in the limiting case of flat plate airfoils where the wing is at zero angle of attack with the flap retracted, we have $\alpha = 0$ and $\delta_F = 0$, which would lead to zero pressure coefficient $C_p = 0$. In that case, the crossflow velocity would be identically zero, as expected. Also, at any stagnation point on the flap where C_p is close to unity, both the chordwise and the crossflow velocity become close to zero, again as expected from the definition of stagnation points. All of these can be regarded as a partial validation of the estimate. Also note that the velocity V is also used in the empirical correlation published in Ref. 5. In that case, a value of V for the Boeing 737 aircraft with flaps deployed at 40 deg is given as $0.4974U_0$. By using the preceding results with α and δ_F taken to be 5 and 40 deg, respectively, and with a typical value of C_p taken as 0.5, we estimate that $V = 0.6088U_0$ very close to that used in Ref. 5.

VI. Results of Regression Analysis

The functional dependency of the noise on the geometrical, operational, and aerodynamic quantities is assumed to follow form (2). The indices of the power laws (b_1, b_2, b_3, ...) are found by correlating the overall sound pressure levels (OASPL) at the overhead position (90 deg) with these parameters by standard linear regression analysis. This leads to a set of indices for each of the components, which are summarized in Table 2. These are the correlation parameters common to all of the components. There are also parameters unique to each individual component. For example, the flap side-edge noise is also related to the strength of the side-edge vortex and to the velocity of the spanwise flow. For the two side edges, the results for these two parameters are given in Table 3. A cautious note about the linear regression analysis is that the results, namely, the indices of the power laws (b_1, b_2, b_3, ...), would be unique if the parameters on the right hand side of Eq. (2) were truly independent of each other. This is apparently not the case here, and some of the parameters in Eq. (2) are clearly coupled to each other aerodynamically. For example, the lift of the wing is a function of the angle of attack. Because both parameters appear on the right-hand side of Eq. (2), their individual contribution to the noise may not be uniquely revealed by the regression analysis. At this stage, we are unable to resolve this issue and have to leave it to future research.

Table 2 Summary of indices in Eq. (2)

Coefficient	Aileron	Inboard (IB) flap	Outboard (OB) flap	Slat
S_0	37.3	0.65	0.86	219.8
b_1	5.8	5.3	5.3	5.6
b_2	3.36	0.05	0.05	4.45
b_3	3.46	1.78	4.12	1.15
b_4	3.46	0.0	0.0	1.03
b_5	3.36	2.02	2.02	0.0

Table 3 Indices for flap side-edge nosie

Coefficient	IB flap	OB flap
Γ	0.12	0.21
V	0.11	0.11

Table 4 Coefficients of the normalized spectra

Coefficient	Aileron	IB flap	OB flap	Slat
a_0	−14.05	−13.18	−14.51	−12.73
a_1	9.02	10.03	9.20	4.05
a_2	−6.04	−9.41	−4.79	−4.30
a_3	−4.33	−6.62	−3.89	−1.85
a_4	2.11	4.10	1.32	0.19
a_5	0.57	1.42	0.41	0.22
a_6	−0.71	−1.07	−0.59	−0.40

The results given in Tables 2 and 3 determine the functional dependencies of the OASPL on the geometrical, operational, and aerodynamic parameters. The frequency dependence is then found by subtracting the OASPL from the data sets and then fitting the data in terms of a sixth-order polynomial equation. This leads to normalized spectra as a function of the Strouhal number. A general form used in the curve fitting is

$$10\log\{F(Sr)\} = \sum_{n=0}^{6} a_n \{\log(Sr)\}^n \tag{13}$$

where $F(Sr)$ is the spectral function defined in Eq. (2) and the Strouhal number Sr is given by Eq. (3). The coefficients in this equation are given in Table 4. To illustrate, Fig. 10 shows two examples of the normalized data sets for the outboard flap side-edge noise and the slat noise. For both cases, the data include all of the configurations, and the smooth curve is the results of Eq. (13). It is clear from Fig. 10 that the data collapse quite well around about unity Strouhal number, but discrepancies are noticeable at both high and low Strouhal numbers. This may be an indication that more than one curve should be used to collapse the data, which means that there may be more than one major sources for each component. For example, the slat noise may come from both the cove vortex fluctuations and the gap flow fluctuations, each contribute differently in different frequency domains. In this case, each source would correlate to different geometric and flow parameters. This decomposition in frequency is not done here, but will be pursued later.

VII. Validation of Prediction Method

To validate the prediction model developed, comparisons were made with flight-test data. The noise of each component was computed, and then all components were summed to obtain the total noise. The addition of the components is performed on an energy

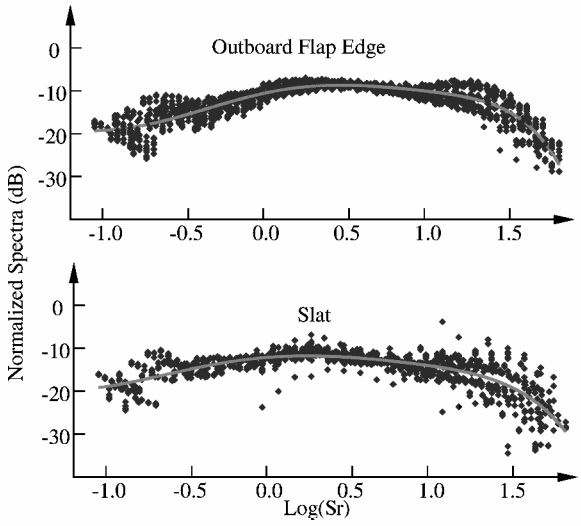

Fig. 10 Normalized spectra for the outboard flap side edge and the slat sources.

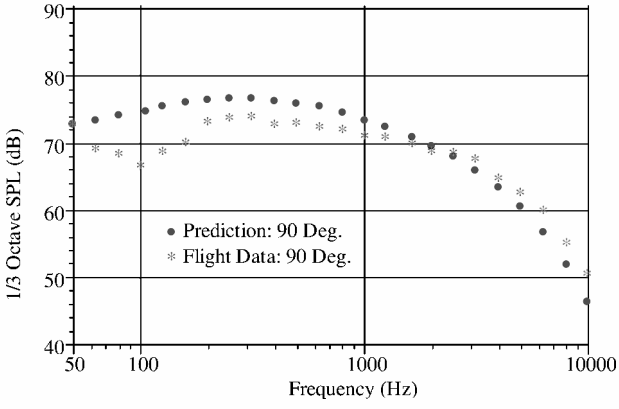

Fig. 11 Comparison between prediction and flight data for Boeing 737 airframe noise at overhead position (394 ft) with $M = 0.238$, $\delta_F = 40$ deg, and landing gear up.

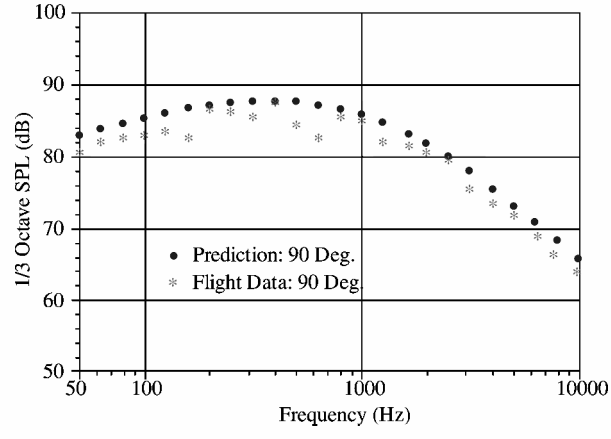

Fig. 12 Comparison between prediction and flight data for DC-10 airframe noise at overhead position (394 ft) with $M = 0.26$, $\delta_F = 50$ deg, and landing gear up.

basis, implying that the sources of the components are assumed to be incoherent and statistically independent of each other, which is a reasonable assumption for airframe noise. Two examples are shown in Figs. 11 and 12, both for approach configurations at aircraft noise certification conditions. Figure 11 shows flight-test data vs predictions comparison for the Boeing 737 airplane and Fig. 12 for the DC-10 airplane. For both cases, reasonably good agreement is noted. The present model seems to capture general features of airframe noise. The good agreement shown in Figs. 11 and 12 is perhaps expected because both the Boeing 737 and the DC-10 airplanes are in the database used to develop the empirical codes. For aircraft configurations outside the database, we think the codes should yield satisfactory result as well because the component-based nature of the method, provided that the configurations of components are within the parameter ranges in the database.

VIII. Conclusions

We have presented the development of a component-based empirical tool for airframe noise prediction. In comparison with previously developed empirical methods, there are many advances in the present approach. One is that the component-based approach relies on a new classification of the noise sources, which is made feasible by recent progress in airframe noise research. For example, flap side-edge noise is now commonly known as one of the dominant contributors to the total airframe noise. Thus, this component is emphasized in the prediction tool developed here, in contrast to previous models that emphasized more trailing-edge noise. Another advance in our method is that the prediction tools are derived from data correlation for all of the individual components, which is again in contrast to previous methods that divide the total noise into components but have to rely on modeling for each component. This is because recent developments in phased microphone array measurements have made it feasible to find the noise sources for individual components, whereas for conventional measurements by free-field microphones, source separation is very difficult and not practical. The present approach is also more physics based. This is because the predictions are made not only from airplane gross dimensions and gross flow parameters, but also from local flow quantities that are directly responsible for noise generation. This incorporates the cause-and-effect relations of sound generation in the empirical method and represents a step forward in airframe noise prediction. It also points to directions of noise reduction by reducing the source strength. For example, the roll-up vortex at the flap side edge is identified as the main source of flap side-edge noise. It generates noise by unsteady oscillations and by scattering of vortical energy into sound at the sharp corners of the flap side edge. With this understanding, potential noise reduction concepts can be developed by either reducing the vortex strength or moving the vortex away from the sharp corners.

As discussed earlier, there remain many unresolved issues related to the empirical approach presented here, some of which deal with very fundamental aspects of aerodynamic noise research that may impact much more than just empirical prediction. For example, the measurement technique of phased microphone arrays has shown wide applications in many branches of aeroacoustics, but there is still no reliable way of converting array measurements into far-field noise spectra. Because of this, an empirical approach has been utilized in this paper with calibration that heavily relies on other measurement techniques. Another issue is whether there is significant Reynolds number effect in small-scale model tests, the progress of which would definitely benefit not only empirical tool development, but also our fundamental understanding of the airframe noise sources.

We have presented the methodology of developing the component-based empirical tool and have given details for the flap side-edge component. The methodology is clearly also applicable to all of the other components in the aircraft high-lift system. For example, we have postulated that slat noise is very likely related to the slat cove vortex, the geometry of the gap flow between the slat trailing edge and the main wing, and the gap flow. It is then desirable to correlate slat noise to quantities related to these features.

Acknowledgments

A large part of the database used in this paper was collected under the NASA Advanced Subsonic Technology Program and the development of the empirical model was partially funded by NASA with R. A. Golub as Technical Monitor. The authors wish to thank R. A. Golub for his support. R. Sen, B. Hardy, G. Miller, and M. Donelson

of The Boeing Company were involved in the work described here and made valuable contributions.

References

[1]Bauer, A. B., and Munson, A. G., "Airframe Noise of the DC-9-31," NASA CR 3027, 1978.

[2]Fink, M. R., "Airframe Noise Prediction Method," Federal Aviation Administration, Rept. FAA-RD-77-29, 1979.

[3]Fink, M. R., "Noise Component Method for Airframe Noise," *Journal of Aircraft*, Vol. 16, No. 10, 1979, pp. 659–665.

[4]Yamamoto, K. J., Donelson, M. J., Huang, S. C., and Joshi, M. C., "Airframe Noise Prediction Evaluation," NASA CR 4695, 1995.

[5]Yee, P., Underbrink, J. R., Sen, R., Kusunose, K., Dougherty, R., and Blackner, A. M., "Airframe Noise Generation and Radiation," NASA Contract Report, 1996.

[6]Guo, Y. P., Joshi, M., Bent, P., and Yamamoto, K., "Surface Pressure Fluctuations on Aircraft Flaps and Their Correlation with Far Field Noise," *Journal of Fluid Mechanics*, Vol. 415, 2000, pp. 175–202.

[7]Guo, Y. P., and Joshi, M. C., "Noise Characteristics of Aircraft High Lift Systems," *AIAA Journal*, Vo. 41, No. 7, 2003, pp. 1247–1256.

[8]Guo, Y. P., "A Model for Slat Noise Generation," AIAA Paper 97-1647, May 1997.

[9]Guo, Y. P., "Prediction of Flap Edge Noise," AIAA Paper 99-1804, June 1999.

[10]Crighton, D. G., "Airframe Noise," *Aeroacoustics of Flight Vehicles: Theory and Practice*, NASA RP-1258, Vol. 1, 1991, pp. 391–447.

[11]Hardin, J. C., "Noise Radiation from the Side Edges of Flaps," *AIAA Journal*, Vol. 18, No. 5, 1980.

[12]Sen, R., "Local Dynamics and Acoustics in a Simple 2D Model of Airfoil Lateral-Edge Noise," AIAA Paper 96-1673, May 1996.

[13]Khorrami, M. R., Singer, B. A., and Radeztsky, R. H., "Reynolds Averaged Navier–Stokes Computations of a Flap Side-Edge Flow Field," AIAA Paper 98-0768, June 1998.

[14]Meadows, K. R., Brooks, T. F., Humphery, W. M., Hunter, W. H., and Gerhold, C. H., "Aeroacoustic Measurements of a Wing Flap Configuration," AIAA Paper 97-1595, May 1997.

[15]Mosher, M., "Phased Arrays for Aeroacoustic Testing: Theoretical Development," AIAA Paper 96-1713, May 1996.

[16]Soderman, P. T., and Noble, S. C., "Directional Microphone Array for Acoustic Studies of Wind Tunnel Models," *Journal of Aircraft*, 1975, pp. 169–173.

[17]Brooks, T. F., Marcolini, M. A., and Pope, D. S., "A Directional Array Approach for the Measurement of Rotor Noise Source Distributions with Controlled Spatial Resolution," *Journal of Sound and Vibration*, Vol. 112, No. 1, 1987, pp. 192–197.

[18]Hayes, J. A., Horne, W. C., Soderman, P. T., and Bent, P. H., "Measurement of Reynolds Number Effect on Airframe Noise in the 12-Foot Pressure Wind Tunnel," AIAA Paper 99-1959, May 1999.

[19]Guo, Y. P., Stoker, B., Hardy, B. A., Bent, P., and Joshi, M. C., "DC-10/MD-11 Acoustic Test in NASA Ames 12-ft Pressurized Wind Tunnel," NASA CR CRAD-9310-TR-4894, 1998.

[20]Hayes, J. A., Horne, W. C., Soderman, P. T., and Bent, P. H. "Airframe Noise Characteristics of a 4.7% Scale DC-10 Model," AIAA Paper 97-1594, June 1997.

[21]Allen, C. S., and Soderman, P. T., "Scaling and Extrapolating Small-Scale In-Flow Wind Tunnel Jet Noise to Full Scale Fly-Over Jet Noise," AIAA Paper 97-1602, June 1997.

[22]Blake, W. K., *Mechanics of Flow-Induced Sound and Vibration*, Academic Press, 1986.